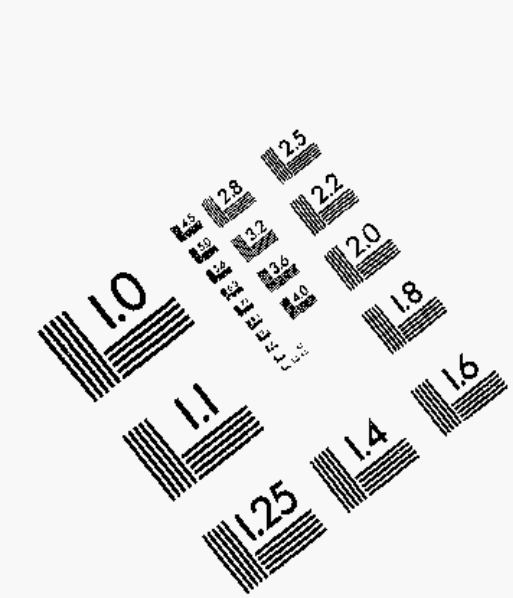

Association for Information and Image Management

1100 Wayne Avenue, Suite 1100
Silver Spring, Maryland 20910
301/587-8202

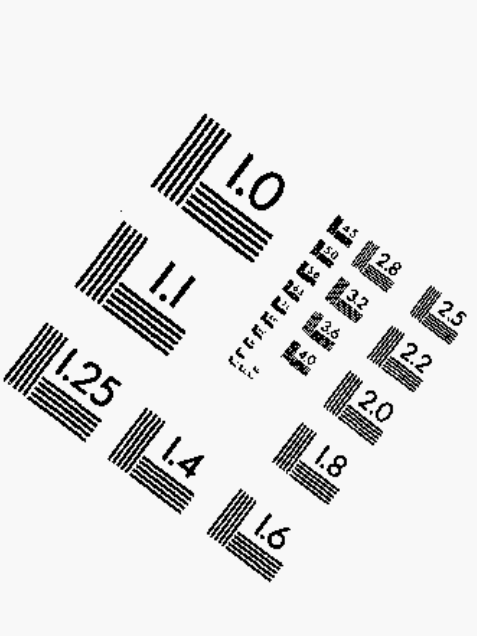

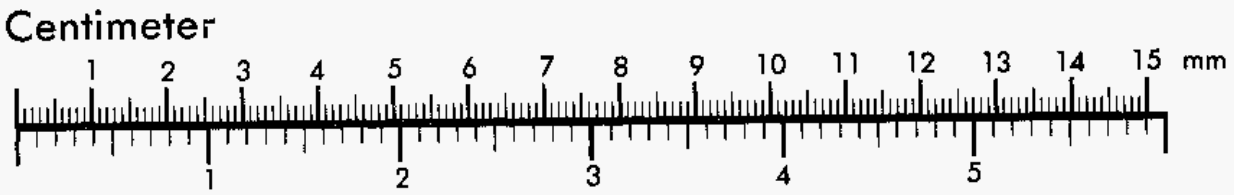

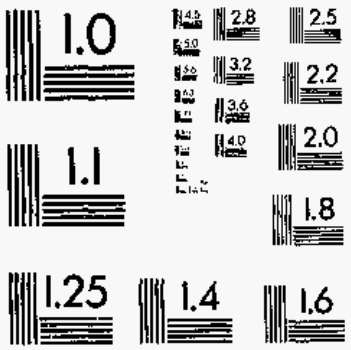

MANUFACTURED TO AIIM STANDARDS
BY APPLIED IMAGE, INC.

1 of 1

2

CONF-940449--14

UCRL-JC-117416
PREPRINT

Multi-Use Applications of Dual-Band Infrared (DBIR) Thermal Imaging for Detecting Obscured Structural Defects

N. K. Del Grande and P. F. Durbin

This paper was prepared for submittal to the SPIE Conference on Underground & Obscured Object Imaging & Detection, Orlando, Florida, April 4-8, 1994

May 1994

Lawrence Livermore National Laboratory

Multi-use applications of dual-band infrared (DBIR) thermal imaging for detecting obscured structural defects

Nancy K. Del Grande and Philip F. Durbin
Lawrence Livermore National Laboratory
P. O. Box 808, Livermore CA 94550
Telephone: (510) 422-1010
Fax: (510) 422-3834

ABSTRACT

Precise dual-band infrared (DBIR) thermal imaging provides a useful diagnostic tool for wide-area detection of defects from corrosion damage in metal airframes, heat damage in composite structures and structural damage in concrete bridge decks. We use DBIR image ratios to enhance surface temperature contrast, remove surface emissivity noise and increase signal-to-clutter ratios. We clarify interpretation of hidden defect sites by distinguishing temperature differences at defect sites from emissivity differences at clutter sites. This reduces the probability of false calls associated with misinterpreted image data. For airframe inspections, we map flash-heated defects in metal structures. The surface temperature rise above ambient at corrosion-thinned sites correlates with the percentage of material loss from corrosion thinning. For flash-heated composite structures, we measure the temperature-time history which relates to the depth and extent of heat damage. In preparation for bridge deck inspections, we map the natural day and night temperature variations at known concrete slab delamination sites which heat and cool at different rates than their surroundings. The above-ambient daytime and below-ambient nightime delamination site temperature differences correlate with the volume of replaced concrete at the delamination sites.

1.0 APPLICATION OF FLASH-HEATED DBIR THERMAL IMAGING FOR AIRFRAMES

During the well-publicized Aloha Airlines accident, damage from corrosion caused the aircraft skin to rip apart from the Boeing 737 airframe. To maintain aircraft reliability, the Air Force spends over $700M annually for corrosion-related maintenance actions. To mitigate airframe corrosion damage, the Federal Aviation Administration (FAA) Technical Center sponsors R&D within the Aging Aircraft Nondestructive Inspection (NDI) Technology Research and Development Program.

In 1993, the FAA Aging Aircraft NDI Technology Program supported thermal infrared imaging efforts at Wayne State University (WSU) and LLNL. WSU uses a single band infrared (SBIR) technique for thermal-wave imaging of corrosion and disbonds within flash-heated aircraft structures.[1] LLNL uses a dual-band infrared (DBIR) technique to provide quantitative corrosion damage detection within flash-heated airframes.[2-5] We use DBIR image ratios, to improve temperature contrast, remove clutter and quantify corrosion damage within aircraft structures.

Our advanced development approach (patent pending)[6] would provide an early warning of low-level (5% or 6%) material-loss effects from corrosion thinning. This approach, if successful, will provide a rapid, safe, reliable, wide-area, corrosion-detection and imaging tool for in situ, non-intrusive inspections of large structures. This tool does not presently exist. It would address the need for early warning signals of incipient corrosion damage and minimize the cost for corrosion repair in airframes.

During 1993, we inspected the Boeing 737 Jetliner at the FAA/AANC (Aging Aircraft NDI Center) Test Bed Facility at Sandia/Albuquerque NM. We detected and quantified corrosion-related, thickness losses which occurred within the lap splice of the flash-heated Boeing 737 aircraft skin. Our dynamic temperature and thermal-inertia maps depicted corrosion pockets, inside a lap splice, which was situated beneath the galley and the latrine. We photographed "pillowing" at this site, which inferred the expansion of corrosion by-products within the riveted lap splice. Below, we discuss our mapping procedures and the results of this demonstration.[7]

2.0 EMISSIVITY-CORRECTED AIRFRAME TEMPERATURE MAPS

Using DBIR image ratios (from DBIR cameras which scan flash-heated targets at infrared wavelengths of 3-5 μm and 8-12 μm) we enhance surface temperature contrast and remove the mask of surface emissivity clutter (from dirt, dents, markings,

tape, sealants, uneven paint, paint stripper, exposed metal and roughness variations). This clarifies interpretation of subtle heat flow anomalies associated with hidden defects and corrosion. We compute DBIR image ratios of high-contrast temperature (T^5) and emissivity-ratio (E-ratio) maps, based on an expansion of Planck's radiation law,[8] which has been used successfully for other applications: [9-20]

$$(\mathbf{T}/\mathbf{T}_{av})^5 = (\mathbf{S}/\mathbf{S}_{av}) / (\mathbf{L}/\mathbf{L}_{av}) \quad (1)$$

$$\mathbf{E\text{-}ratio} = (\mathbf{L}/\mathbf{L}_{av})^2 / (\mathbf{S}/\mathbf{S}_{av}) \quad (2)$$

where **S** is the short-wavelength intensity (e.g., $\mathbf{I}_5$), $\mathbf{S}_{av}$ is the average value of the pixels in **S**, **L** is the long wavelength intensity (e.g., $\mathbf{I}_{10}$) and $\mathbf{L}_{av}$ is the average value of the pixels in **L**. See Figure 1 for the Boeing 737 images of the above ambient lap splice temperature and emissivity-ratio maps which allowed us to distinguish corrosion-related thickness loss effects from surface emissivity clutter.

3.0 DYNAMIC AIRFRAME TEMPERATURE CHANGES FOR FLASH-HEATED LAP SPLICE

Corrosion within the Boeing 737 (epoxy-bonded) lap splice causes disbonding. Trapped by-products of corrosion act like an insulator, delaying heat transfer by conduction from the front to the back surface. This effect is shown in Figure 2 by the near-constant temperature contrast at 0.4 s, 0.8 s and 1.6 s after onset of the heat flash, based on our measurements of the FAA/AANC owned Boeing 737 aircraft inspected at the Sandia Test Bed Facility hangar in Albuquerque, New Mexico.

Corrosion-related material loss effects are measured at 0.4 seconds after the heat flash. Temperatures at 0.4 s are sensitive to material loss effects within a lap splice and insensitive to timing uncertainties. The timing is early enough to provide a good temperature contrast for sites with and without material loss from corrosion. At later times, trapped materials mask the temperature-time history which characterizes material-loss effects for corrosion sites.

We established the correlation between percent thickness loss and above-ambient surface temperature rise, at 0.4 seconds after the heat flash, based on our measurements for five specimens which averaged a 24 ± 5 % thickness loss per °C temperature rise. These specimens included a F-18 partially corroded wing box (with a 2.9 mm uncorroded thickness) and four 1.0 mm to 3.9 mm thickness aluminum panels with milled flat-bottom holes which had thickness losses ranging from 6% to 62%.

4.0 THERMAL INERTIA MAPPING FOR AIRFRAME CORROSION DAMAGE DETECTION

We developed thermal inertia (or effusivity) maps, which have been used previously for other applications, [21,22] by solving the heat transfer equation for a thick panel with an instantaneous surface heat flux: [23,24]

$$T(x,t) = \frac{q}{\sqrt{4\pi k\rho c t}} \exp\left(-\frac{x^2}{4\alpha t}\right) \quad (3)$$

where T is temperature, x is the distance from the surface, k is thermal conductivity, ρ is density, c is heat capacity, α is thermal diffusivity, t is time and q is the surface heat flux. For a semi-infinite solid approximation, the surface temperature is proportional to the inverse square root of time. In practice, we map the fuselage composite thermal inertia, $(kpc)^{1/2}$, based on the (inverse) slope of the surface temperature versus inverse square root of time. Composite thermal inertia maps characterize shallow skin defects within the lap splice at early times (<0.3 s) and deeper skin defects within the lap splice at late times (>0.4 s). Late time composite thermal inertia maps depict where corrosion-related thickness losses occur based on temperature versus time histories recorded from 0.4 to 3.2 s.

We note in Figure 3 (right side) a butterfly-like pattern at the upper right side. This is where the corrosive activity invaded the inside (upper lap edge) of the Boeing 737 lap splice on Stringer 26, near station F400.7, beneath the galley and the latrine. Typical visible signs of corrosion were also evident (e.g., pillowing) resulting from the increased volume of corrosion by-products within the lap splice, between the rivet heads.

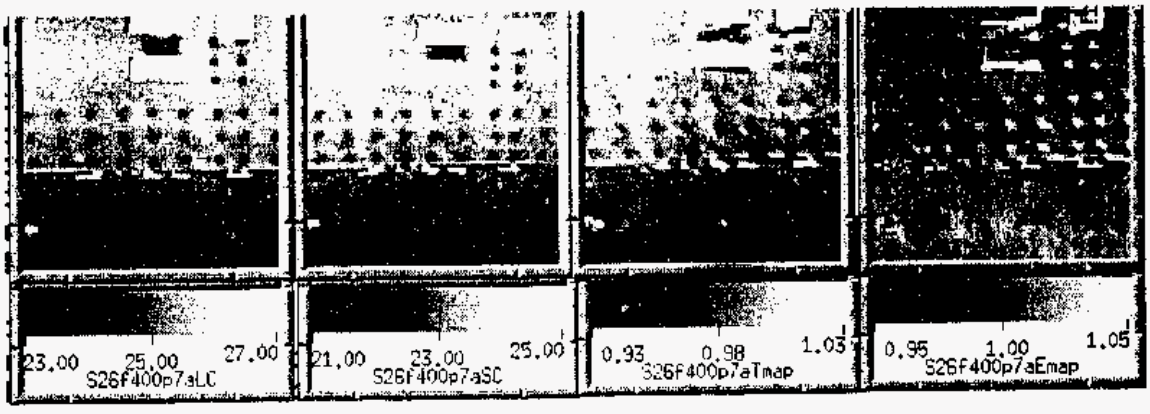

Figure 1. Boeing 737 lap splice structure with hidden defects showing maps (left to right) of 10 μm and 5 μm apparent temperatures (°C), dual-band infrared (DBIR) high-contrast temperatures and emissivity-ratio differences from surface clutter.

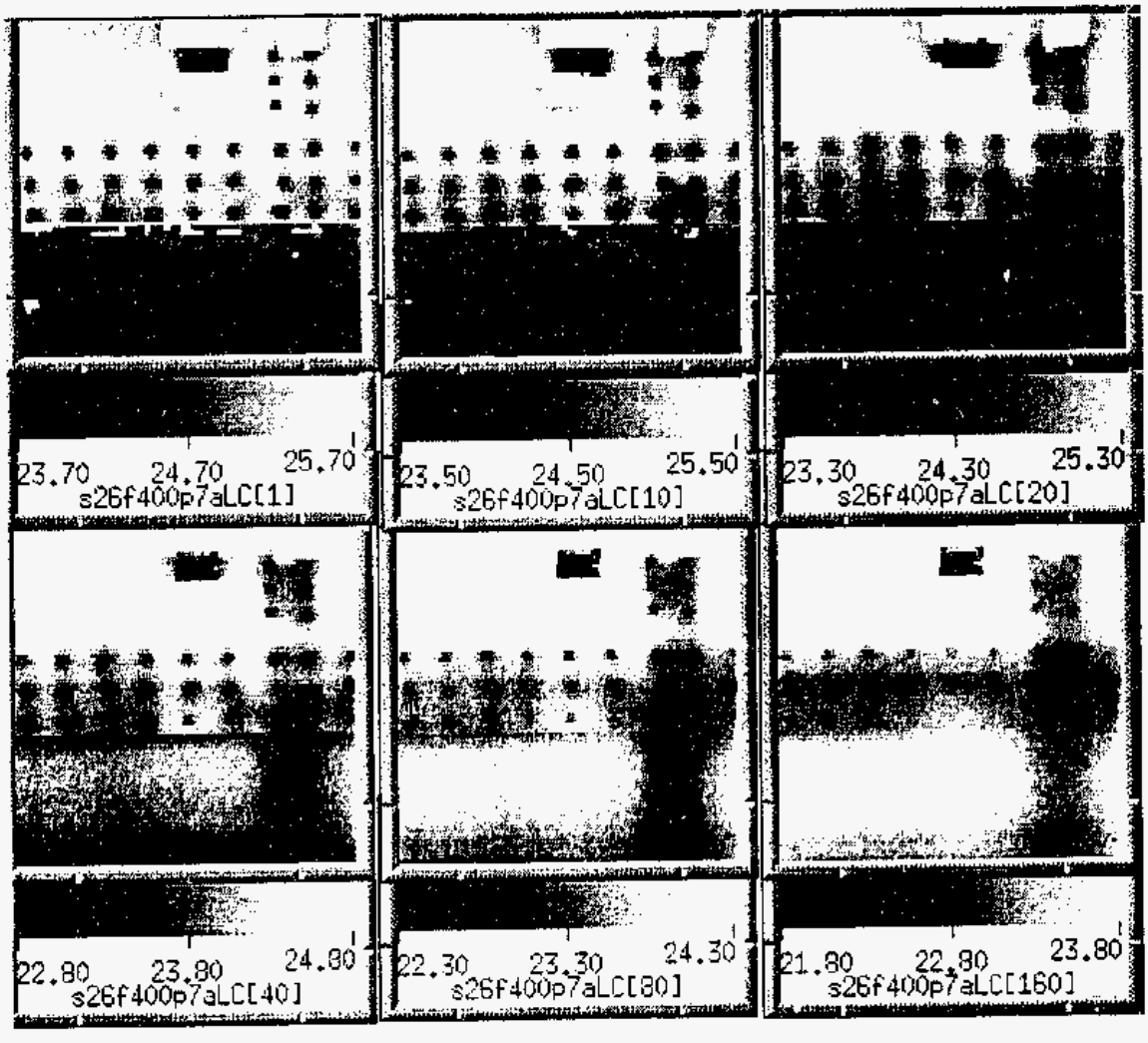

Figure 2. The dynamic temperature variations for the Boeing 737 lap splice images at 0.04 s, 0.4 s and 0.8 s (top left to right) and at 1.6 s, 3.2 s and 6.4 s (bottom left to right) based on the 10 μm apparent temperature maps.

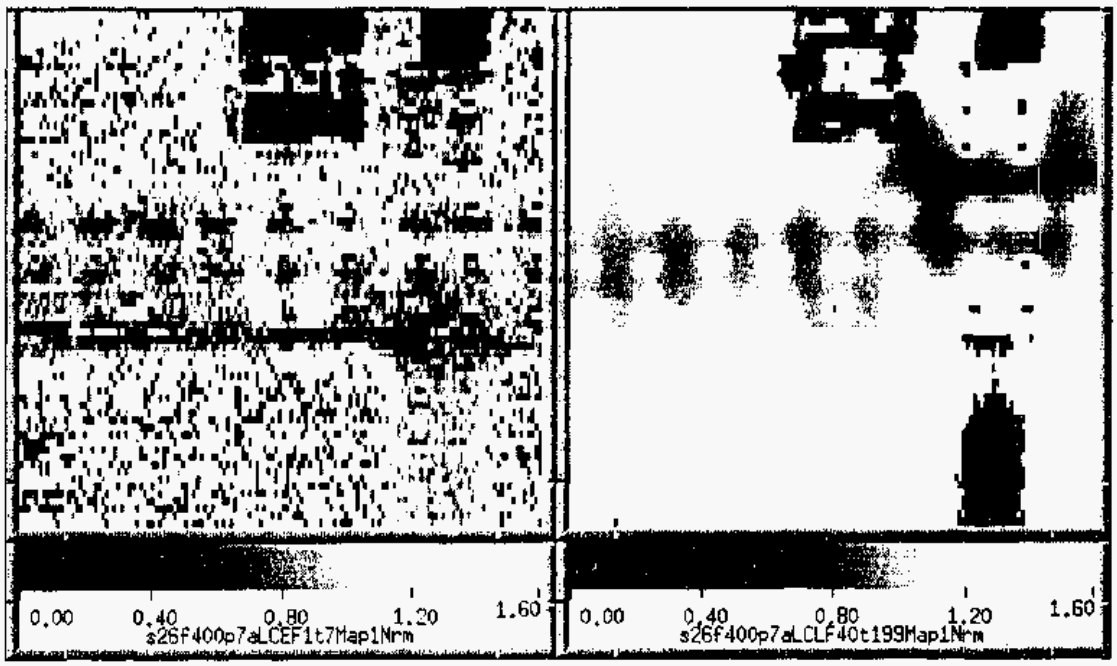

Figure 3. Seven early-time (less than 0.28 s, on the left) and 159 late-time (1.6 s to 8.0 s, on the right) images were used to produce composite thermal inertia maps of the Boeing 737 aircraft fuselage lap splice shown above. Note the relatively low thermal inertia for the front-surface cloth tape and masking tape markers (top center and right corner) and the back surface tear strap (bottom right corner).

5.0 APPLICATION OF FLASH-HEATED DBIR THERMAL IMAGING FOR COMPOSITES

We investigated heat damage at the upper rim center of a graphite epoxy dome seen at the left side of Figure 4. Two white (hot) lobes have temperatures above 70 ^{0}C as seen at 0.040 s after onset of the heat flash on the left and again (enlarged) at the upper left corner or four detailed pictures on the right side of Figure 4. The remaining three detailed pictures show changes in heat damage with depth inferred by dynamic changes in the relative thermal inertia of the heat-damaged zone. The heat damage was caused by applying heat from a hot-air gun during a prolonged period of time.

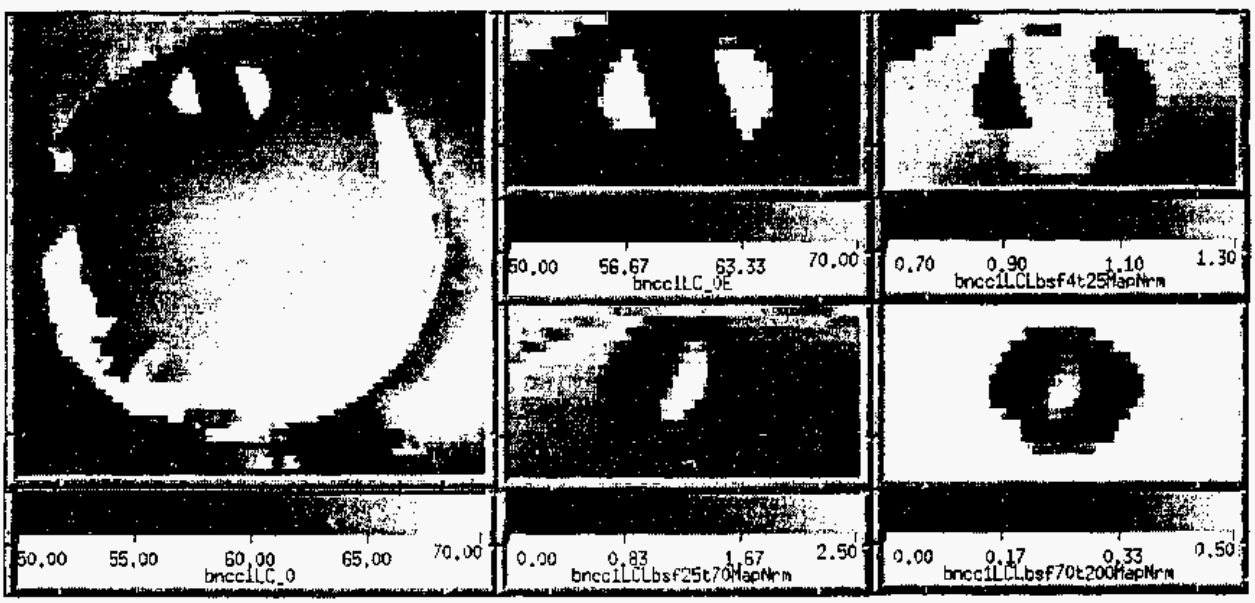

Figure 4. Thermal infrared inferred temperature maps of a graphite-epoxy dome, at left, with thermal, top center, and thermal inertia maps, at top right, bottom center and bottom right showing heat damaged lobes from shallow to deeper dome layers.

Adjacent at the upper right corner is an early-time thermal inertia map showing shallow layer heat damage. This map was a reconstruction of the temperature-time history taken at early times from 0.2 s to 1.0 s after the heat flash. The black lobes have the least thermal inertia (resistance to temperature change) at heat-damaged sites which reached the hottest temperatures. At intermediate times (1 s to 3 s) the low (black) thermal inertia zone had a circular perimeter which enclosed both lobes and a smaller undamaged center (lower center). At late times (3 s to 8 s) the diameter of the heat-damaged zone decreased.

6.0 APPLICATION OF DBIR THERMAL IMAGING FOR CONCRETE STRUCTURES

Two square, 1.8 m (6 feet) on-a-side, concrete test slabs A and B were cast with five variable size styrofoam implants, 5.1 cm (2 inches) below the surface, representing delamination sites in surrogate concrete bridge deck structures. Each slab was 19.0 cm (7.5 inches) thick. See Figures 5, 6, 7, 8 and 9. The dimensions and average daytime minus nighttime surface temperature differences relative to the surroundings, ΔT, for styrofoam delaminations 1 through 5 (note clockwise positions) were:

(1) 22.9 cm (9 inches) on-a-side, 0.32 cm (1/8 inch) thick, volume = 166.0 cm^3 (10.1 in^3); $\Delta T = 3.63 \pm 0.55$ ^oC
(2) 15.2 cm (6 inches) on-a-side, 0.32 cm (1/8 inch) thick, volume = 73.7 cm^3 (4.5 in^3); $\Delta T = 2.03 \pm 0.24$ ^oC
(3) 10.2 cm (4 inches) on-a-side, 0.32 cm (1/8 inch) thick, volume = 32.8 cm^3 (2.0 in^3); $\Delta T = 1.23 \pm 0.49$ ^oC
(4) 10.2 cm (4 inches) on-a-side, 0.79 cm (5/16 inch) thick, volume = 81.9 cm^3 (5.0 in^3); $\Delta T = 1.73 \pm 0.45$ ^oC
(5) 10.2 cm (4 inches) on-a-side, 1.43 cm (9/16 inch) thick, volume = 147.0 cm^3 (9.0 in^3); $\Delta T = 1.97 \pm 0.32$ ^oC

In addition, thermistor probes recorded surface and subsurface temperatures (e.g., above and below the styrofoam at X, at three shallow depths at Y and at the surface at Z). Also, consecutive alphabetic letters shown counterclockwise along the slab perimeter mark the sites of surface object clutter shown on the diagram of Figure 5.

(A) rusty steel pan with hole at center placed at top left side of slab;
(B) wood painted white at top with grease at bottom placed at bottom left side of slab;
(C) stainless steel plate placed at bottom center of slab;
(D) plastic road markers placed at bottom right of slab;
(E) rock placed at top right of slab.

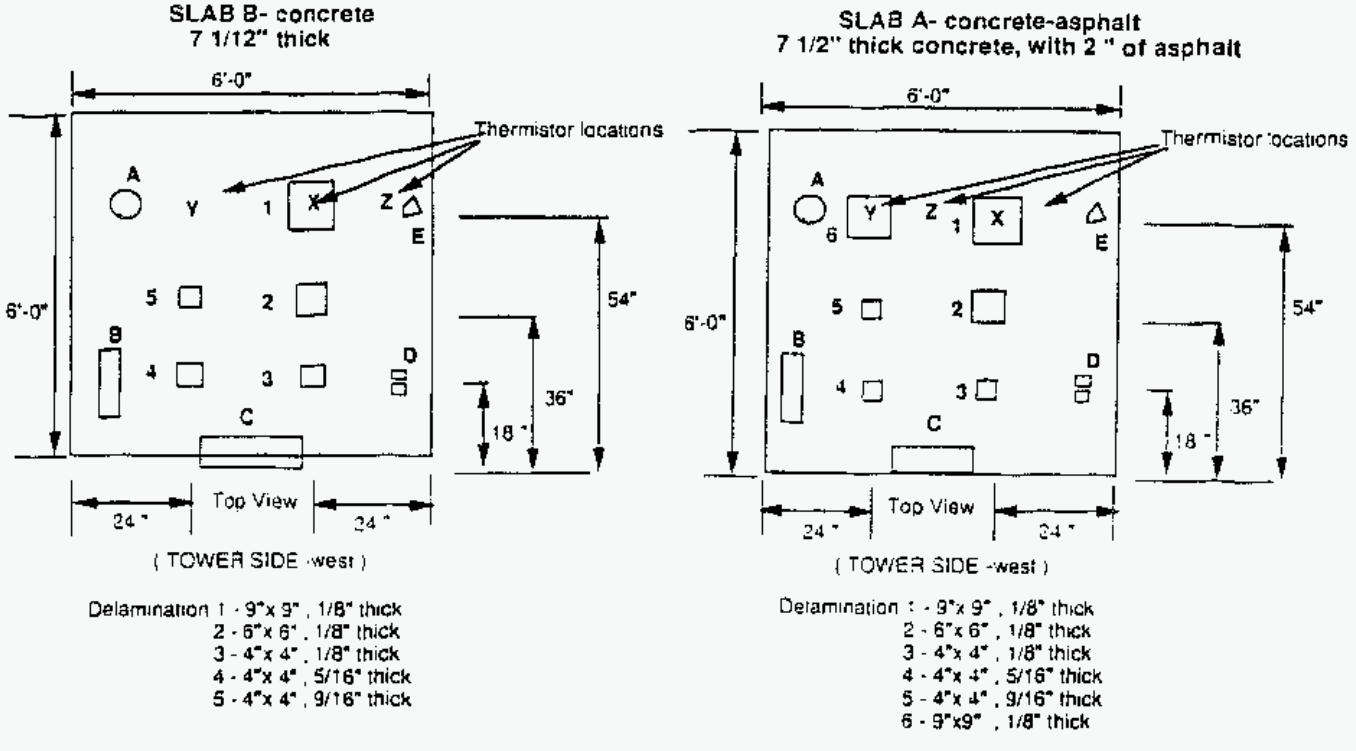

Figure 5. Diagram of concrete slabs used to measure the effects of subsurface delamination sites for a concrete bridge deck.

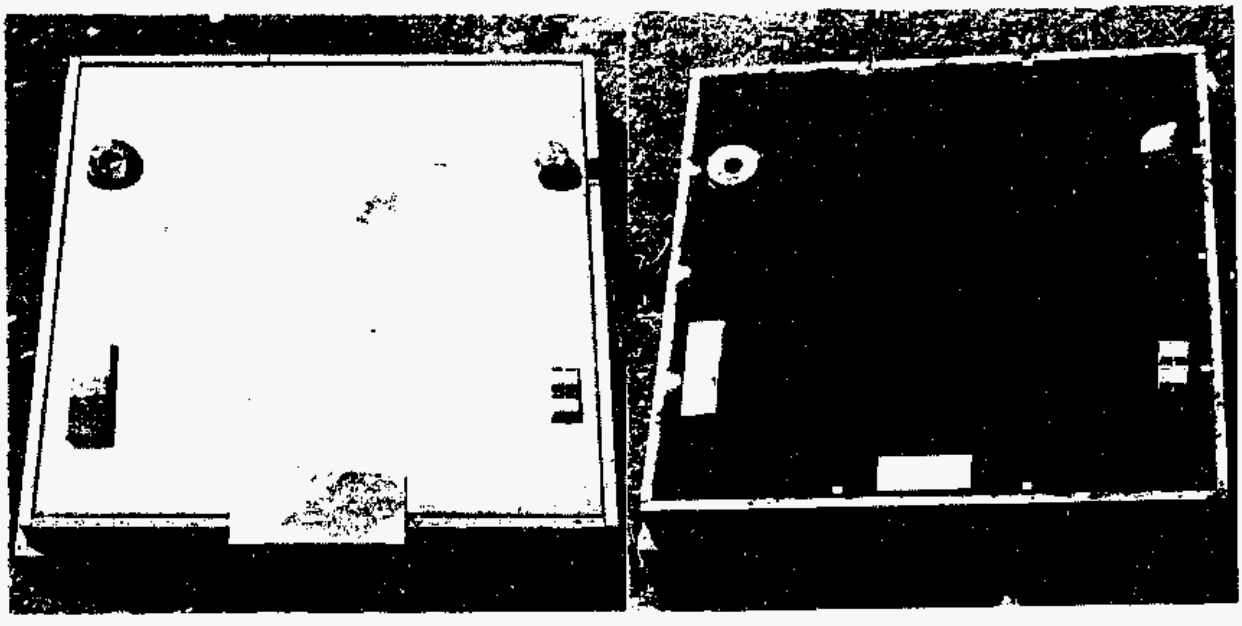

Figure 6. Photos: left, showing concrete slab B with five subsurface styrofoam delamination sites and five clutter sites along perimeter; and right, showing similar concrete slab A covered by 5.1 cm (2 inches) asphalt with a delamination site at the asphalt-concrete interface located at top, center-left, above the same size concrete delamination site #1 at top, center-right.

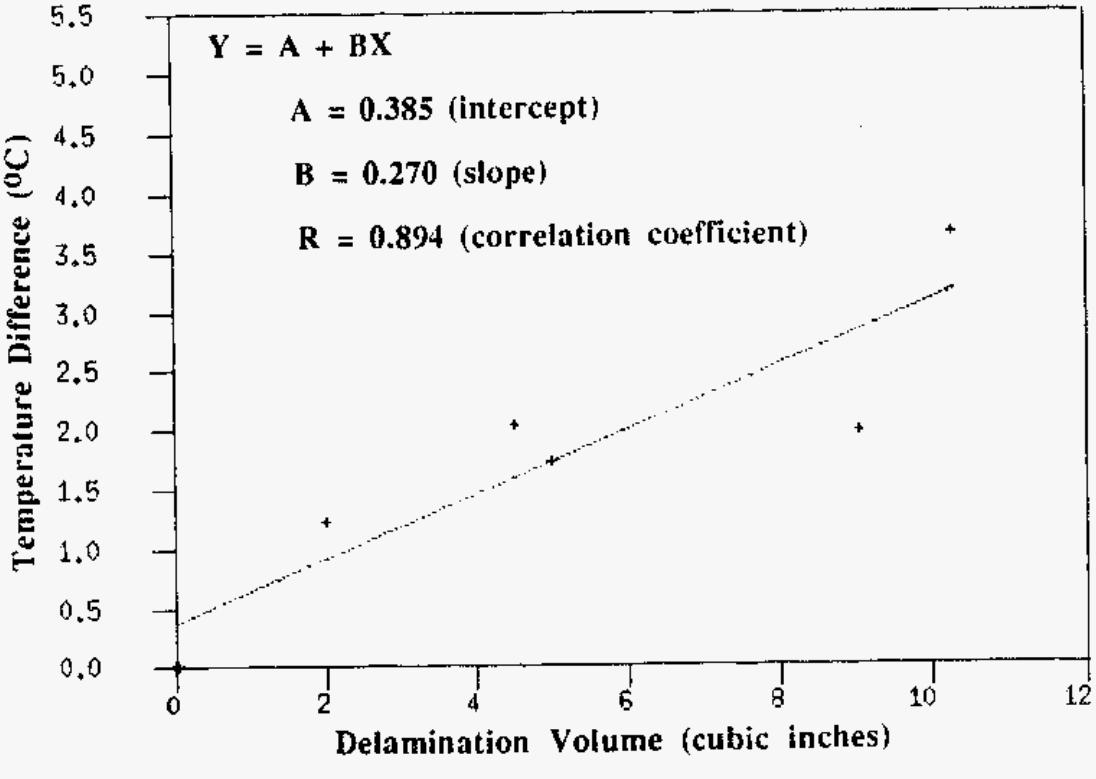

Figure 7. Average daytime (above ambient) minus nighttime (below ambient) temperature differences vary as volume of styrofoam inserts from DBIR data taken for two concrete slabs, January 29, 1994, and for one concrete slab, April 12, 1994.

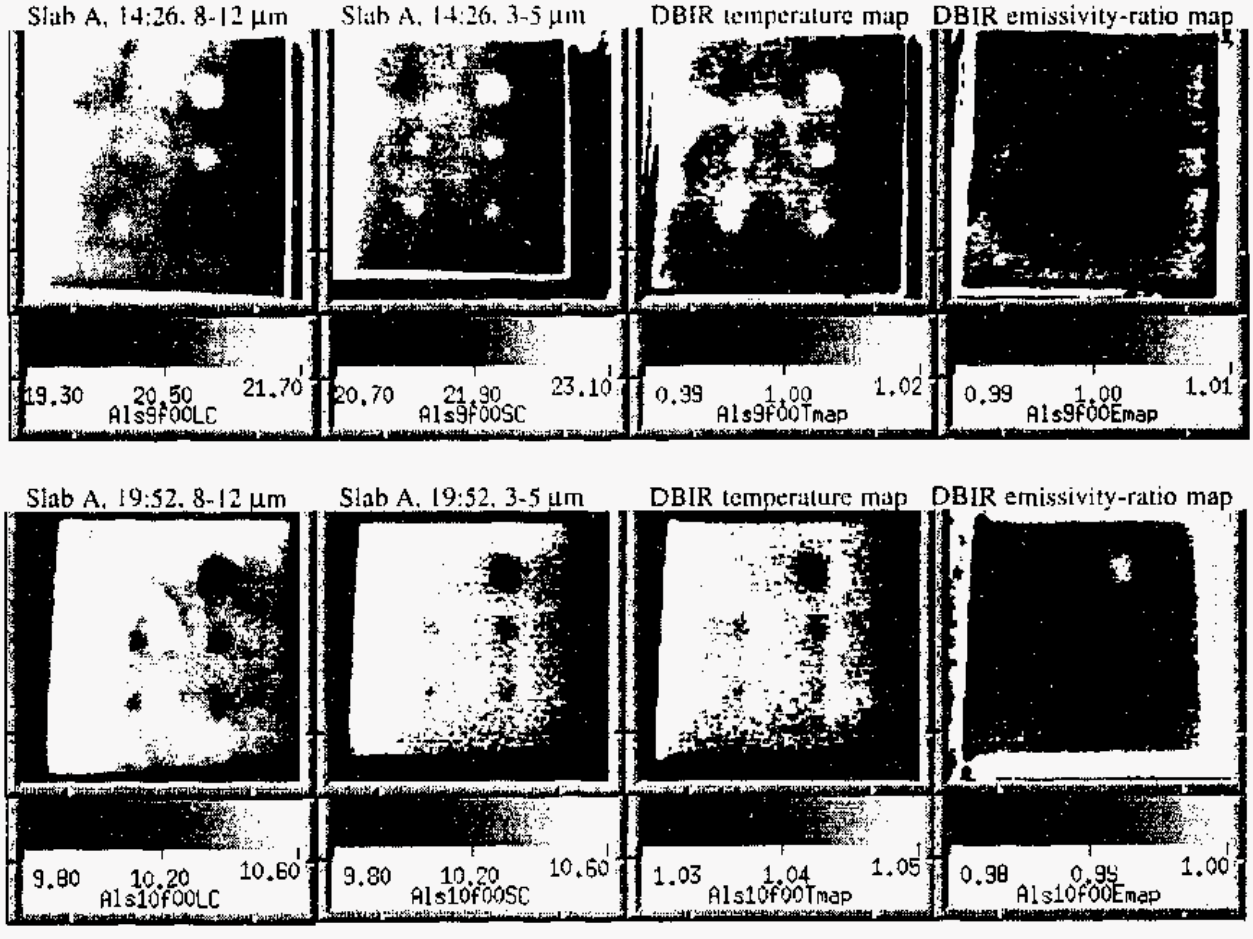

Figure 8. January 29, 1994 DBIR images recorded for concrete Slab A without asphalt and surface clutter. Apparent temperature maps are in °C. High-contrast DBIR temperature and emissivity-ratio maps (relative scale) show warmer than ambient daytime delamination site, and cooler than ambient nighttime delamination site, temperature gradients. Note that the emissivity-ratio maps show neither delamination sites nor clutter sites, in the absence of surface clutter.

7.0 IMPLICATIONS OF CONCRETE SLAB DEMONSTRATIONS

The images shown in Figures 8 and 9 have similar temperature maps which differ significantly from their respective DBIR emissivity-ratio maps. DBIR emissivity-ratio maps do not show surface temperature gradients associated with subsurface delamination sites. Instead, they locate emissivity-ratio variations associated with surface clutter (DBIR emissivity variations on the surface of the concrete from staining or surface objects e.g., in Figure 9). By tagging the sites of surface clutter, we are able to remove these sites from the high-contrast surface temperature maps.

The April 12, 1994 apparent temperature and DBIR high-contrast temperature maps of concrete Slab B images (see Figure 9, top two rows) show the five clutter sites along the perimeter, the five delamination site positions seen in Fig. 5, and one emissivity-ratio anomaly, near the center of the daytime and nighttime DBIR images of Slab B. The sites of surface clutter on these images are tagged amd removed using the corresponding positions of clutter sites found on the emissivity-ratio maps.

The April 12, 1994 apparent temperature and DBIR high-contrast temperature maps of asphalt-covered concrete Slab A (see Figure 9, bottom two rows) show one major delamination site for a 23 cm (9 inch) on-a-side delamination placed at top, left-of-center, at the concrete-asphalt interface, but not directly above the concrete delamination sites shown in Figure 8. Also, there are less pronounced indications of at least one of the deeper delamination sites within the concrete. The DBIR emissivity-ratio maps do not show surface temperature gradients associated with subsurface delamination sites. Instead, they locate emissivity-ratio variations associated with the five large surface objects along the perimeter and asphalt-like compounds encasing three small thermistors.

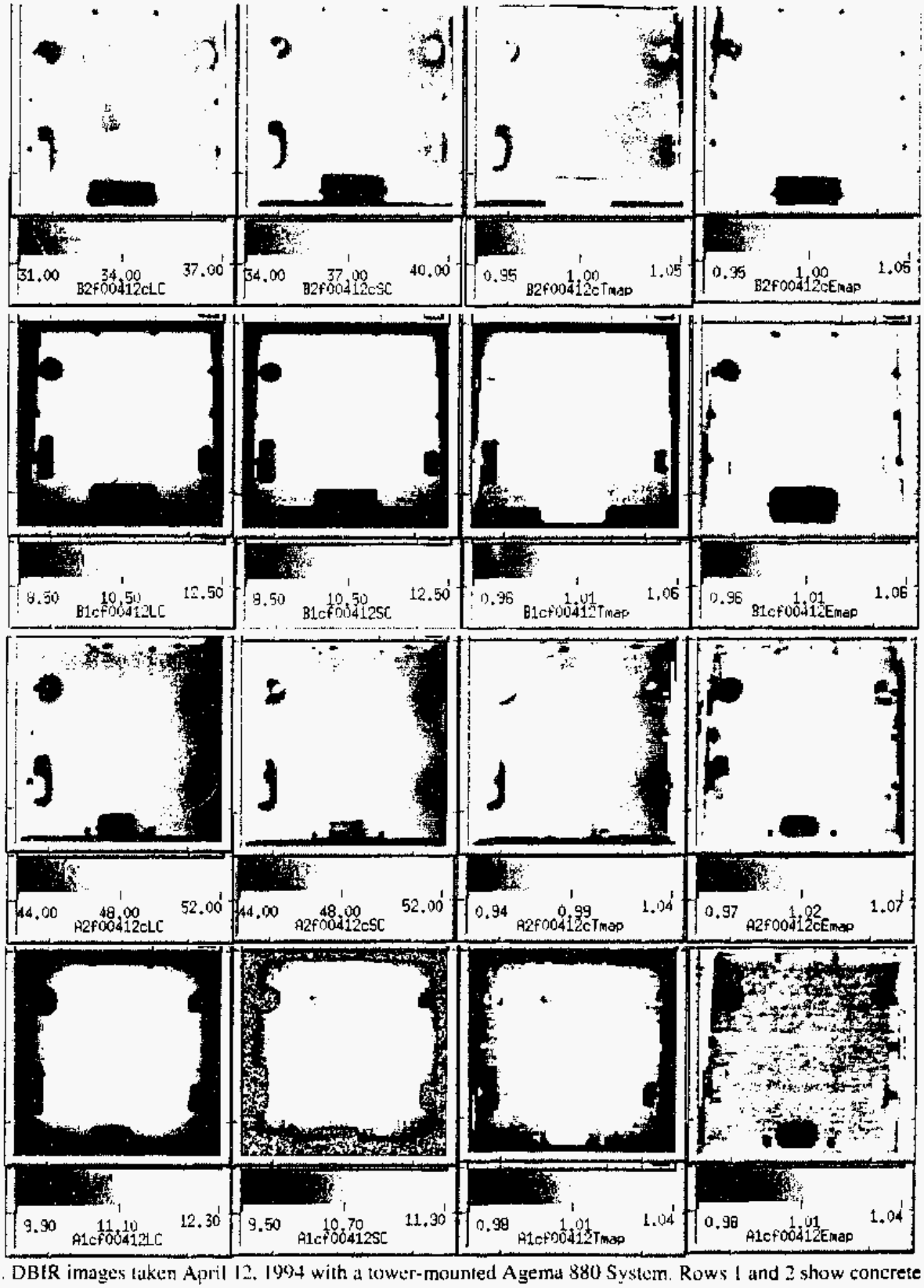

Figure 9. DBIR images taken April 12, 1994 with a tower-mounted Agema 880 System. Rows 1 and 2 show concrete Slab B at 14:50 and 06:02 respectively. Rows 3 and 4 show asphalt-covered concrete Slab A at 14:36 and 06:17 respectively. Apparent temperature maps were recorded at 8-12 μm (column 1) and at 3-5 μm (column 2). High-contrast temperature maps (column 3) show both delamination and clutter sites, whereas emissivity-ratio maps (column 4) show only clutter sites.

8.0 SUMMARY, CONCLUSIONS AND FUTURE PLANS

DBIR ratios of 3-5 and 8-12 μm heat-stimulated, coregistered airframe images, provide separate temperature and emissivity-ratio maps to improve the defect site signal-to-noise and clarify interpretation of corrosion damage. We established the relationship between a 1 ^{o}C temperature rise (0.4 s after the heat flash) and a 24 % thickness loss from corrosion. The emissivity-ratio map enables us to remove the surface clutter sites which have spatially varying emissivity differences.

Surface clutter occurs from roughness variations, dirt, dents, uneven paint, sealants, stripper materials, cleaner residues, metal markers, tape and ink. The use of emissivity-ratio maps to identify (then remove) clutter sites on co-registered temperature maps is unique at LLNL. It significantly improves the signal-to-noise (S/N) for siting corrosion damage, compared to the S/N achievable with SBIR methods. It clarifies interpretation of corrosion damage by removing the mask from clutter.

Thermal inertia maps image corrosion damage in metal structures and heat damage in composites. These maps are based on the temperature-time history of the flash-heated target described by Eq. (3) where temperatures vary as the inverse square root of time. Damage sites have a larger temperature spread and less thermal inertia (i.e., resistance to temperature change) than their surroundings.

Visually, it is difficult to distinguish whether bulges on the airframe skin result from excessive use of sealants, production ripples or pillowing produced by expansion from corrosion by-products. To classify defect types, we are studying rapidly-varying temperatures which occur at 0 to 30 ms after the heat flash. By correctly classifying defect types, we expect to reduce the probability of false corrosion calls, which occur when corrosion damage is confused for something else.

To inspect composite structures for under-curing, over-heating, over-pressurizing or impact damage, we use thermal inertia maps at early (0.2 to 1.0 s), intermediate (1 s to 3 s) and late (3 s to 8 s) times. These maps probe the depth and extent of delaminations in thermoplastic wing patches, teflon inserts in graphite epoxy domes and heat, pressure and impact damage.

To inspect concrete bridge decks which are covered (or not) by asphalt, we will adapt DBIR thermal imaging from a moving vehicle. We expect shallow concrete delamination sites more than 23 cm (9 inches) on-a-side, to produce direct or indirect surface thermal footprints either from the displaced volume of concrete or the ensuing damage at the asphalt-concrete interface.

9.0 ACKNOWLEDGMENTS

This work was performed by LLNL under the auspices of DOE contract number W-7405-ENG-48. We acknowledge support from the FAA Aging Aircraft Non-Destructive Inspection R&D Program, Interagency Agreement DTFA03-92-A-00007, the FHWA order number DTFH61-93-Y-00145, and the LLNL Nondestructive Evaluation Thrust Area. We thank Michael Gorvad for valuable technical discussions in the areas of image processing and analysis. We appreciate the support of Satish Kulkarni, Harry Martz, Ken Dolan and Graham Thomas.

10.0 REFERENCES

1. L. D. Favro, P. K. Kuo, R. L. Thomas, T. Ahmed and Y. X. Wang, "Thermal wave imaging of corrosion and disbonds in aircraft structures" in Proceedings of SPIE Conference 2001: Nondestructive Inspection of Aging Aircraft, Ed. Michael T. Valley, Nancy K. Del Grande and Albert S. Kobayashi, San Diego CA (1993).

2. P. F. Durbin, N. K. Del Grande, K. W. Dolan, D. E. Perkins and A. B. Shapiro, "Dual-Band Infrared Thermography for Quantitative Nondestructive Evaluation" Joint Army, Navy, NASA, Air Force (JANNAF) NDE Subcommittee Meeting Proceedings, Apr. (1993).

3. N. K. Del Grande, K. W. Dolan, P. F. Durbin, M. R. Gorvad, B. T. Kornblum, D. E. Perkins, D. J. Schneberk and A. B. Shapiro, "Three-Dimensional Dynamic Thermal Imaging of Structural Flaws by Dual-band Infrared Computed Tomography" in Proceedings of SPIE Conference 1942: Underground and Obscured Object Imaging and Detection, Ed. Nancy Del Grande, Ivan Cindrich and Peter Johnson, Orlando FL (1993).

4. N. K. Del Grande, K. W. Dolan, P. F. Durbin, M. R. Gorvad and A. B. Shapiro, "Dynamic thermal tomography for nondestructive inspection of aging aircraft" in Proceedings of SPIE Conference 2001: Nondestructive Inspection of Aging Aircraft, Ed. Michael T. Valley, Nancy K. Del Grande and Albert S. Kobayashi, San Diego CA (1993).

5. N. K. Del Grande, "Dual Band Infrared Imaging for Quantitative Corrosion Detection in Aging Aircraft", Proceedings of the American Society for Nondestructive Testing (ASNT) Meeting, Nov. (1993).

6. N. K. Del Grande, K. W. Dolan, P. F. Durbin and D. E. Perkins, "Emissivity-Corrected Infrared Method for Imaging Anomalous Structural Heat Flows", Patent Pending (1994).

7. N. K. Del Grande, K. W. Dolan, P. F. Durbin, M. R. Gorvad and A. B. Shapiro, "Dual-Band Infrared (DBIR) Imaging Inspections of Boeing 737 and KC-135 Aircraft Panels", UCRL Report: Interagency Agreement DTFA03-92-A-0007 (1993).

8. L. A. LeSchack and N. K. Del Grande, "A Dual-Wavelength Thermal Infrared Scanner As A Potential Airborne Geophysical Exploration Tool", see Appendix for derivation of Eq. (1) and Eq. (2), Geophysics 41, 1318 (1976).

9. Philip Durbin and Nancy Del Grande, "Dual-Band Infrared Imaging For Concrete Bridge Deck Inspection", Proceedings of Structural Materials Technology-An NDT Conference, Atlantic City NJ, Feb. (1994).

10. N. K. Del Grande, P. F. Durbin and D. E. Perkins, "Dual-Band Infrared Imaging Applications: Locating Buried Minefields, Mapping Sea Ice, And Inspecting Aging Aircraft", Review of Progress in Quantitative Nondestructive Evaluation, Ed. D. O. Thompson and D. E. Chimenti, Plenum Pr. NY, 12A, 465-472, (1993).

11. John E. Lewis, Nancy Del Grande, Ian McKendry, Philip Durbin and Matti Lepparanta, "Thermal Mapping" in ERS-1 Baltic Sea Ice Calibration/Validation Post-Experiment Report / Pipor/Finland, Finnish Institute of Marine Research Report 1992 (9), Ed. Matti Lepparanta and Mikko Lensu, Helsinki (1992).

12. N. K. Del Grande, P. F. Durbin, M. R. Gorvad, D. E. Perkins, G. A. Clark, J. E. Hernandez and R. J. Sherwood, "Dual-band Infrared Capabilities for Imaging Buried Object Sites" in Proceedings of SPIE Conference 1942: Underground and Obscured Object Imaging and Detection, Ed. Nancy Del Grande, Ivan Cindrich and Peter Johnson, Orlando FL (1993).

13. G. A. Clark, J. E. Hernandez, S. K. Sengupta, R. J. Sherwood, P. C. Schaich, M. R. Buhl, R. J. Kane, M. J. Barth, N. K. Del Grande, "Sensor Feature Fusion for Detecting Buried Objects", Proceedings of SPIE Conference 1942: Underground and Obscured Object Imaging and Detection, Ed. Nancy Del Grande, Ivan Cindrich and Peter Johnson, Orlando FL (1993).

14. Nancy Del Grande, "Airborne Detection Of Buried Minefields", Energy and Technology Review, University of California LLNL Report, UCRL-52000-91-12. (1991).

15. N. K. Del Grande, G. A. Clark, P. F. Durbin, D. J. Fields, J. E. Hernandez and R. J. Sherwood, "Buried Object Remote Detection For Law Enforcement", Surveillance Technologies, SPIE Vol. 1479, 335 (1991).

16. N. K. Del Grande, "Sensor Fusion Methodology for Remote Detection of Buried Land Mines", Proceedings of the 3rd National Symposium on Sensor Fusion, Orlando, Fl, Vol. 1, IIAC/ERIM, p.407, August (1990).

17. N. K. Del Grande, "Temperature Evaluated Mine Position Survey (TEMPS) Application of Dual Band Infrared Methodology", Proceedings of the 1990 Meeting of the IRIS Specialty Group on Passive Sensors, IRIA/ERIM sponsored symposium, March (1990).

18. N. K. Del Grande, "Airborne Temperature Survey Maps of Heat Flow Anomalies for Exploration Geology", Proceeding of International Symposium on Remote Sensing of Environment, Second Thematic Conference on Remote Sensing for Exploration Geology, Dec. 1982. Reprinted in Geothermal Resources Council Bulletin 14, p.3, Mar. (1985).

19. N. Del Grande, "Airborne and Field Temperature Surveys Compared At Long Valley KGRA, California", Geothermal Resources Council Transactions 5, 71 (1978).

20. N. K. Del Grande, "Method for Identifying Anomalous Terrestrial Heat Flows"; Patent No. 4,005,289, (1977).

21. E. G. Grinzato, C. Bressan, P. G. Bison, A. Mazzoldi, P. Baggio, C. Bonacina, "Evaluation of moisture content in porous material by dynamic energy balance", Proceedings of SPIE Conference 1682: Thermosense XIV, Ed. Jan K. Eklund, Orlando FL p. 213, (1992).

22. Ph. M. Delpech, D. M. Boscher, F. Lepoutre, A. A. Deom and D. L. Balageas, "Quantitative nondestructive evaluation of carbon-carbon composites by pulsed infrared thermography", in Review of Progress in Quantitative Nondestructive Evaluation, 12B, Ed. by Donald O. Thompson and Dale E. Chimenti, Plenum Press, New York and London, p. 1297 (1993).

23. H. S. Carslaw and J. C. Jaeger, Conduction of Heat in Solids, 2nd Edition, Oxford Univ. Pr., London, pp. 101, 112 and 259 (1980).

24. Jane W. Maclachlan Spicer, "Thermographic NDT", SPIE Short Course Notes, SC37, Thermosense '93, Orlando FL Section 5, p. 13 (1993).

DATE
FILMED
10/12/94
END